Influence of mechanical damage on fluid flow patterns investigated using CT scanning imaging and acoustic emissions techniques

Christian David, Beatriz Menendez, Jean-Marie Mengus

Influence of mechanical damage on fluid flow patterns investigated using CT scanning imaging and acoustic emissions techniques

Christian David,[1] Beatriz Menéndez,[1] and Jean-Marie Mengus[2]

Received 6 June 2008; revised 18 July 2008; accepted 23 July 2008; published 29 August 2008.

[1] In order to get some insight into the influence of mechanical deformation on fluid flow patterns, we performed series of X-ray CT scanning runs during capillary imbibition experiments to image the water front displacement in Bentheim sandstone samples. A three steps procedure was followed: 1) intact rock samples were tested, 2) the samples were deformed in creep experiments under triaxial conditions with recording of acoustic emissions, 3) the deformed samples experienced a second capillary imbibition test with CT scanning imaging. Using image analysis tools, relevant flow parameters like the height, velocity and curvature of the water front were measured. Stress-induced damage had a significant impact on the flow patterns. However contrasted results were obtained: localized damage evidenced by acoustic emissions clustering resulted in one experiment in local disturbance of the flow patterns, whereas in the second one a fracture detected by CT scan did not modify the local flow geometry. **Citation:** David, C., B. Menéndez, and J.-M. Mengus (2008), Influence of mechanical damage on fluid flow patterns investigated using CT scanning imaging and acoustic emissions techniques, *Geophys. Res. Lett.*, *35*, L16313, doi:10.1029/2008GL034879.

1. Introduction

[2] Imaging techniques have been widely used to investigate microstructural attributes in porous rocks. Among them X-ray CT scanning methods are of common use to tackle a wide range of problems in geosciences [*Mees et al.*, 2003] like petroleum engineering research [*Van Geet et al.*, 2000], strain localization [*Louis et al.*, 2006], stone decay [*Ruiz de Argandoña et al.*, 1999] and fluid flow [*Clavaud et al.*, 2008] just to mention a few. Whereas many studies have focused on imaging mechanical damage [e.g., *Lenoir et al.*, 2007] and fluid flow processes [e.g., *Clavaud et al.*, 2008], to our knowledge there are no experimental study which intended to use imaging techniques for characterizing fluid flow patterns under mechanical loading, in order to get a better insight into hydromechanical coupling in geomaterials. It has been shown that permeability evolution with stress may be complex [e.g., *Zhu and Wong*, 1997] and that fluid flow can be concentrated in preferential flow paths in heterogeneous porous media [e.g., *David*, 1993]. In particular it is of prime importance to assess whether a fracture or a damaged zone acts as a preferred conduit for fluids in which case an enhancement of the overall permeability is expected in the formation, or as a barrier or a seal which would make the flow paths more tortuous and the reservoir formation less permeable. Because imaging fluid flow during mechanical testing is a difficult task, we developed a three stage methodology combining X-ray CT scanning on intact rock samples, creep tests with acoustic emissions recording for localization of induced damage [*Fortin et al.*, 2006], and again X-ray CT scanning on the damaged samples after unloading. Doing so we intend to address the following questions. What is the influence of damage on fluid flow? Do localized damage zones (like fractures) act as preferential flow paths or barriers? More generally is localized damage associated with localized flow patterns?

2. Methodology

[3] The key point in our methodology is to conduct capillary imbibition experiments under a medical CT scanner in order to image fluid flow patterns in real time experiments. A typical run proceeds as follows. A dry core sample (80 mm long, 40 mm diameter) is placed on a stand inside a container, such that the bottom surface of the sample is at the same altitude as the top surface of the container. The contact area with the stand can be considered as negligible. Water supplied by a reservoir is then allowed to enter into the container from the bottom, at a flow rate slow enough to allow the operator to get out of the room before starting the CT scanning. Once the water reaches the bottom of the sample, capillary rise starts and water enters into the rock sample. The medical scanner records one single image of the central cross-section of the core sample every 2.5 seconds, which is the fastest rate available. The resolution of the scanner used in our experiment is about 400 μm. The selected rock is Bentheim sandstone, a quartz-rich sandstone with a mean grain size of about 200 μm, a porosity of 23% and a permeability of about 10^{-12} m^2. The total duration of a typical run is about 7 minutes, and the number of images taken is about 180. A raw image is shown in Figure 1a. The region were water has invaded the sample is brighter because the bulk density has increased (like in medical radiographs where bones appear in white and flesh in dark). The capillary front has a curvature and can fairly well be described by an arc of a circle. Notice the dark areas on each side at the bottom, which are artefacts introduced by the stand on which the sample is installed (beam hardening effect). In order to make the analysis easier, we use image analysis tools to enhance the contrast between dry and wet regions (Figure 1b). Doing so we obtain a

[1] Université Cergy-Pontoise, Département des Sciences de la Terre, UMR7072, CNRS, Cergy-Pontoise, France.
[2] Institut Français du Pétrole, Rueil-Malmaison, France.

0094-8276/08/2008GL034879

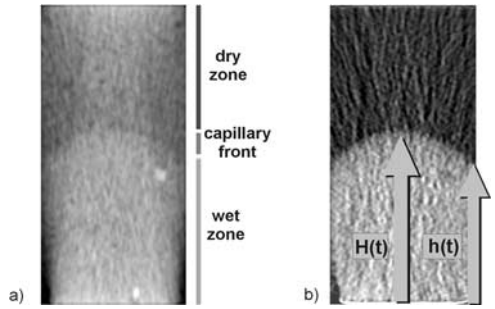

Figure 1. (a) Raw image at an intermediate stage of capillary imbibition. (b) Image with enhanced contrast obtained by subtracting the image of the sample in dry state, from which heights H(t) and h(t) are measured.

modified image on which it is easy to measure several experimental parameters.

3. Experimental Parameters From Image Analysis

[4] We implemented an automatic procedure to estimate the height $H(t)$ of the water front in the center and the height $h(t)$ at the border (Figure 1b) at time t on all images. From these parameters we can calculate the vertical front velocity $v(t) = dH/dt$ and the radius of curvature $\rho(t)$ assuming that the interface can be approximated by an arc of a circle:

$$\rho(t) = \frac{(H(t) - h(t))^2 + R^2}{2(H(t) - h(t))} \quad (1)$$

where R is the radius of the core sample. Figure 2 shows the typical evolution of the water front height vs. time in the center (in black) and at the border (in grey) for intact samples. Symbols correspond to measurements on the series of images, thick lines are fitting curves. The height of the water front at the border always lags behind that in the center, and the height difference keeps on increasing. Consequently the radius of curvature ρ of the interface decreases (Figure 2b). The lower velocity at the border is due to the free boundary condition leading to a reduced driving force for capillary imbibition. The velocity v of the moving interface decreases significantly with time (Figure 2b), in agreement with the capillary theory which predicts that H scales as the square root of time. The small increase of the velocity at the end of the experiment is probably an artefact due to boundary effects on the images. The velocity decrease (Figure 2b) is a consequence of the reduction in the magnitude of the driving force. Indeed we can estimate the Darcy velocity $\vec{U} = -\frac{k}{\eta}\left(\overrightarrow{\nabla p} - \rho_w \vec{g}\right)$ where k is the permeability, η, ρ_w and p are the viscosity, density and pressure of the water respectively, and g is gravity. The magnitude of the pressure gradient can be estimated far from the sample boundaries by the ratio of capillary pressure over the height of the moving front, leading to the following relation for the driving force:

$$\left|\vec{F}\right| = \frac{2\gamma\cos(\theta)}{rH} - \rho_w g \quad (2)$$

where γ is the surface tension of the water-air interface, θ is the contact angle (commonly taken to be 0°) and r is an "effective" pore radius. For the radius r we use the results of mercury injection tests conducted on Bentheim sandstone which show a narrow pore entry spectrum with a clear peak at r = 13.2 μm: taking this value into account in equation (2), we calculate a Darcy velocity at mid height U = 0.29 mm/s, in good agreement with the velocity derived from the image analysis (v = 0.35 mm/s, Figure 2b).

4. Mechanical Tests

[5] After having completed the imbibition experiments on intact samples, some of them were selected, dried, then

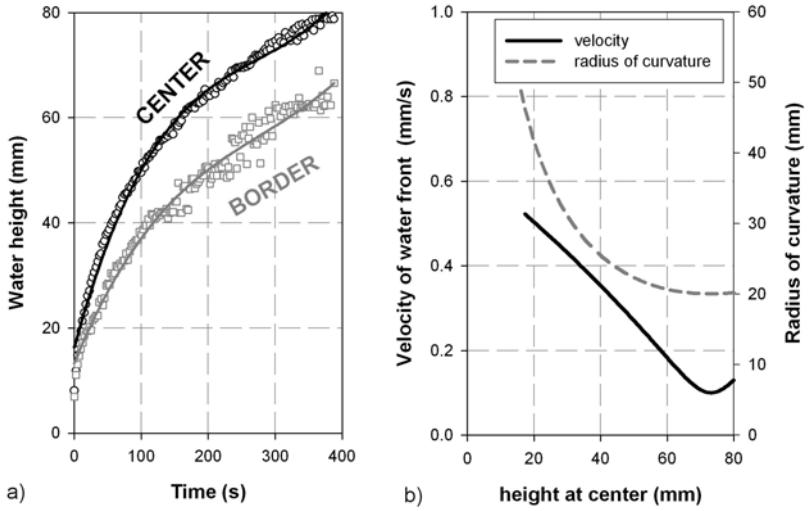

Figure 2. Measured parameters for an intact Bentheim sandstone sample. (a) Water height in the center (black) and on the border (gray) vs. time. Symbols are for measurements on the images, lines are for fitting curves (third power polynomial function). (b) Velocity (solid black) and radius of curvature (dashed grey) vs. height at center.

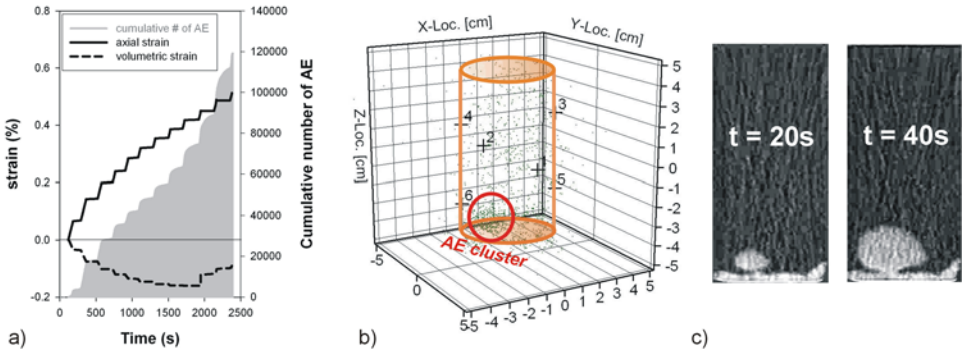

Figure 3. Mechanical and capillary imbibition data for sample BNT#1. (a) Evolution of axial strain (solid black), volumetric strain (dashed black) and acoustic emission activity (grey) for the triaxial creep test. (b) Location of acoustic emissions (small dots) and piezoelectrical transducers (numbered crosses) in the sample. (c) Two images showing the water invasion in the deformed sample after respectively 20 and 40 seconds experiment.

fully saturated with distilled water under vacuum and tested in creep experiments under triaxial conditions with acoustic emissions (AE) recording. We used a 100 kN GDS VIS loading frame and a 15 MPa pressure vessel. A low confining pressure (3 MPa) and pore pressure (1 MPa) was applied in the creep tests. Six acoustic emissions transducers were glued directly on the cylindrical surface of the core samples through holes perforated in the jacket: four transducers were located in a single median plane with one pair of opposite transducers at 1/4th length from the sample bottom and another pair at 1/4th length from the sample top (i.e., 3–4–5–6 in Figure 3b), the last pair of transducers being located at mid height, in the direction orthogonal to the former plane (i.e., 1–2 in Figure 3b), in order to optimize the 3D location of acoustic emissions. A Vallen AMSY-5/6 channels device was used for AE recording. The axial load was increased at constant strain rate (10^{-5} s^{-1}), then the load was held constant at a given level and the sample was allowed to creep for about 10 minutes while recording continuously the acoustic emissions. This procedure was repeated with higher and higher stress levels, and the experiments were stopped before the sample failed by macroscopic fracturing. This is a very sensitive point: because of the fluctuation of the compressive strength due to sample heterogeneity, it is very difficult to assess the maximum stress that a given sample can stand before failure. In fact, with no reliable criteria for stopping the experiment, the sample is unloaded when the operator "feels" a strong acceleration in AE activity by checking changes in the slope of the cumulative AE and by listening to an increase in the background noise on the external speakers of the AE system. We succeeded in doing so in both experiments presented hereafter, whereas some other times we (and the sample) failed.

[6] In Figure 3 we report our results for sample BNT#1. The black lines in Figure 3a gives the evolution of axial (solid line) and volumetric (dashed line) strains vs. time; the steep parts of the curves correspond to axial loading, while the flat parts correspond to the creep stages. Axial strain was given by an external displacement transducer, and volumetric strain was derived from the volume change in the pore pressure system in order to maintain a constant pore pressure. On the same plot we put in grey the cumulative number of AE recorded: more than 10^5 hits in total were recorded by the 6 AE channels. The volumetric strain tells us that the deformation is first compactive, then becomes dilatant, a well-known behaviour of brittle deformation. The evolution of AE activity during the creep stages shows two different trends: at differential stresses below 20 MPa ($t <$ 1000 s) the AE rate is almost constant and low (about 10 hits per second), whereas it strongly increases at higher stresses up to 70 hits per second. In Figure 3b we can see that AE events are distributed throughout the sample, but the most striking feature is that a large number of AE are clustered in the lower part of the sample. However there is no evidence for fracturing as the sample looked undamaged upon unloading. The sample was then dried in an oven, and we conducted a second imbibition experiment under the CT scanner. Interestingly a very different behaviour for the fluid flow patterns was observed. In Figure 3c we show two images taken in the early stages of the capillary rise. Instead of having a smooth curved interface, the water invasion rapidly starts in the region where the cluster of acoustic emissions was detected, giving the image of a "water bubble" growing inside the sample. Notice the very good correlation between the location of the AE cluster (Figure 3b) and the wet region (Figure 3c). At later stages, the water keeps on moving into the rock sample with a water-air interface distorted compared to that of the intact rock.

[7] In Figure 4 we report our results for sample BNT#2. The evolution of axial strain, volumetric strain and acoustic emission activity (not shown here) vs. time was very similar to what we obtained for BNT#1 (Figure 3a). Interestingly the volumetric strain in both experiments was fairly the same when the samples were unloaded (−0.1 %) corresponding to a volume increase in the range 0.1–0.12% in the dilation regime. Like in the previous case, the AE were concentrated in the lower part of the sample (Figure 4a): the difference with BNT#1 is that a fracture that initiated at the lower left corner could be identified at the sample bottom after unloading. This fracture is also nicely imaged by CT scanning in Figure 4b. In order to have a better idea on the geometry of the fracture, a 3D reconstruction of the sample inner structure was done using series of images from a complete CT scan: it revealed two

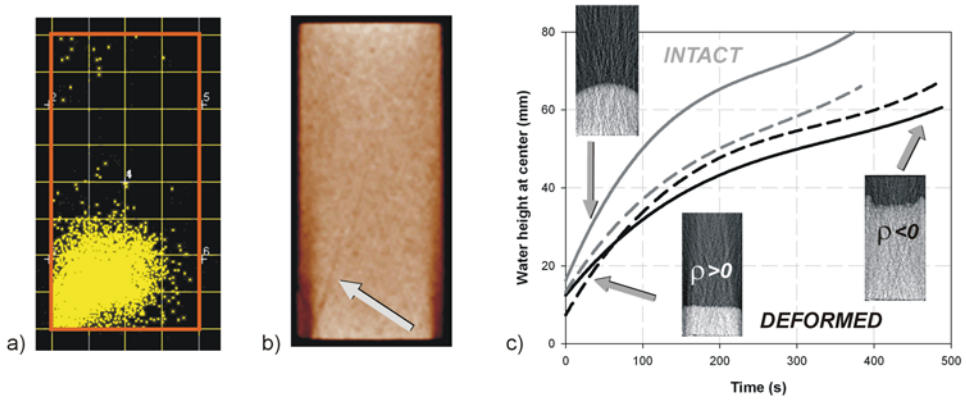

Figure 4. Mechanical and capillary imbibition data for sample BNT#2. (a) Location of acoustic emissions in a central cross-section. (b) Raw image of a scan in the central cross-section: the arrow shows the presence of an incipient fracture. (c) Comparison of the water heights evolution in the intact (grey) and deformed (black) samples. Solid curves are the fitting curves for central height, dashed curves are for fitting curves for the border height.

important features. Firstly the fracture has a conical shape which shows that it was probably created in response to stress concentrations at the boundary between the sample and the metallic sample holder in the pressure vessel, secondly the propagation of the fracture stopped close to the center of the sample, which explains the fact that the sample was still cohesive. In Figure 4c we plotted the evolution of the water front height during imbibition both at the center (solid lines) and on the border (dashed lines), for the intact sample (grey) and the deformed one (black). We can see that at any time the height in the center of the deformed sample is significantly lower than in the intact sample. On the contrary, there is very little difference in the curves relative to the water height on the border. It seems that the changes in the rock properties after mechanical loading are more important in the center of the sample compared to the lateral boundaries. Consequently, the curvature of the capillary fringe is strongly reduced (Figure 4c). Moreover, a transition is observed between a region where the water height at the center is higher than on the border ($\rho > 0$, like for the intact samples), towards a region where the reverse trend is observed ($\rho < 0$). The geometry of the interface in this second region is shown in Figure 4c: the approximation of circular geometry is rather weak, and we do see that the water front in the center clearly lags behind that on the border. In addition, the water-air interface is not smooth, in contrast with what was observed in the intact samples. The last striking result is that during the imbibition process, the fracture which was identified by visual inspection and CT scanning apparently has no influence on the water front geometry: whereas mechanical damage strongly modified the general fluid flow patterns as discussed above, we did not observe any local disturbance in the region where the damage was localized on a fracture, a surprising result for us.

5. Discussion

[8] To summarize, mechanical damage induced in creep tests significantly modified the fluid flow patterns in capillary imbibition experiments run on two samples of Bentheim sandstone. Although both samples were tested in the same experimental conditions, contrasting behaviours were observed, a feature probably due to rock heterogeneity and slight changes in loading conditions. For sample BNT#1, a nice correlation between the growth of a "wetting bubble" and the location of the cluster of AE recorded during the mechanical test was observed, although visual observation and CT scan of the deformed sample did not reveal any macroscopic damage localization. For BNT#2, the fluid flow patterns were also strongly modified, but in a different way: here localized damage along a macroscopic fracture was identified on the CT scan images but the water front in the vicinity of the fracture showed no distortion at all. However major changes were observed at the sample scale with a lower imbibition velocity and curvature of the water-air interface, and an inversion in the curvature of the water front. This latter observation is due to the fact that whereas the velocity is strongly reduced in the center of the sample, it is almost unchanged close to the sample surface, which raises the question of the homogeneity of the deformation inside the sample. The presence of the incipient fracture might be important in this regard, but according to our observations the fracture behaves neither as a drain nor as a barrier, a long-lasting debate in Earth sciences. Is this so because the microstructural attributes of the fracture are not very different from the surrounding rock in terms of pore size distribution ? Only a microstructural study could help to solve this question which we haven't done yet. A microstructural study might also explain why the velocity of the water front in the center is strongly reduced, by about 40% in the early stages (Figure 4c). Assuming that the velocity is proportional to the driving force (equation (2)), a velocity decrease at a fixed height can be explained by a reduction of permeability or an increase of the effective radius r or both. A slight decrease in permeability on the one hand was actually measured on sample BNT#2: before the mechanical loading we measured $k = 1.31\ 10^{-12}$ m^2 and after unloading the creep test we measured $k = 1.23\ 10^{-12}$ m^2 which is not enough to explain the 40% decrease in velocity. An increase in the effective radius on the other hand is consistent with the occurrence of dilatancy during the last creep stages (e.g., Figure 3a for BNT#1). Although we

have some indication that both conditions are met to explain a velocity decrease, one should keep in mind that an increase in pore size is contradictory with a decrease in permeability, unless one takes into account an increase of the tortuosity which would balance the pore size effect. Interestingly, *Baraka-Lokmane et al.* [2001] arrived to a similar discussion on the influence of fracturing on capillary processes in their experiments using magnetic resonance imaging instead of CT scan. In contrast to our results, they observed that open fractures act as preferential drains for fluid flow although the fracture aperture is wider than the typical pore size in the surrounding host rock, thus leading to a capillary driving force with a smaller magnitude. They explain this apparent discrepancy by a difference in wettability between the fracture surface and the pore space outside the fracture that would overcome the aperture effect.

[9] To conclude, the results presented here are part of a more general study involving different rock types, on the influence of heterogeneity, anisotropy, rock microstructure and gravity on capillary processes and fluid flow patterns. A comprehensive set of data will be presented in a future paper.

[10] **Acknowledgments.** This work was supported by IFP thanks to Jean-Marc Daniel. Invaluable technical support was provided by Jean-Marc Siffre and Jean-Christian Colombier in the design of the experimental setup and sample preparation. Many thanks also to Laurent Louis and Ian Main for fruitful discussions, and to both reviewers for valuable comments.

References

Baraka-Lokmane, S., G. Teutsch, and I. G. Main (2001), Influence of open and sealed fractures on fluid flow and water saturation in sandstone cores using magnetic resonance imaging, *Geophys. J. Int.*, *147*, 263–271.

Clavaud, J.-B., A. Maineult, M. Zamora, P. Rasolofosaon, and C. Schlitter (2008), Permeability anisotropy and its relations with porous medium structure, *J. Geophys. Res.*, *113*, B01202, doi:10.1029/2007JB005004.

David, C. (1993), Geometry of flow paths for fluid transport in rocks, *J. Geophys. Res.*, *98*, 12,267–12,278.

Fortin, J., S. Stanchits, G. Dresen, and Y. Guéguen (2006), Acoustic emission and velocities associated with the formation of compaction bands in sandstone, *J. Geophys. Res.*, *111*, B10203, doi:10.1029/2005JB003854.

Lenoir, N., M. Bornert, J. Desrues, P. Besuelle, and G. Viggiani (2007), 3D digital image correlation applied to X-ray micro tomography images from triaxial compression tests on argillaceous rock, *Strain*, *43*, 193–205.

Louis, L., T. F. Wong, P. Baud, and S. Tembe (2006), Imaging strain localization by X-ray computed tomography: Discrete compaction bands in Diemelstadt sandstone, *J. Struct. Geol.*, *28*, 762–775.

Mees, F., R. Swennen, M. Van Geet, and P. Jacobs (2003), *Application of X-Ray Computed Tomography in the Geosciences*, *Geol. Soc. Spec. Publ.*, 215, 1–6.

Ruiz de Argandoña, V. G., A. Rodriguez Rey, C. Celorio, L. M. Suarez del Rio, L. Calleja, and J. Llavona (1999), Characterization by computed X-ray tomography of the evolution of the pore structure of a dolomite rock during freeze-thaw cycling tests, *Phys. Chem. Earth, Part A*, *24*, 633–637.

Van Geet, M., R. Swennen, and M. Wevers (2000), Quantitative analysis of reservoir rocks by microfocus X-ray computerised tomography, *Sediment. Geol.*, *132*, 25–36.

Zhu, W., and T. Wong (1997), The transition from brittle faulting to cataclastic flow: Permeability evolution, *J. Geophys. Res.*, *102*, 3027–3041.

C. David and B. Menéndez, Université Cergy-Pontoise, Département des Sciences de la Terre, UMR7072, CNRS, F-95031 Cergy-Pontoise, France.

J.-M. Mengus, Institut Français du Pétrole, F-92852 Rueil-Malmaison, France. (christian.david@u-cergy.fr)